Original Article

Journal of Intelligent Material Systems and Structures

Journal of Intelligent Material Systems and Structures
1–14

DOI: 10.1177/1045389X16672732
jim.sagepub.com
SAGE

Coupling of experimentally validated electroelastic dynamics and mixing rules formulation for macro-fiber composite piezoelectric structures

Shima Shahab[1] and Alper Erturk[2]

Abstract

Piezoelectric structures have been used in a variety of applications ranging from vibration control and sensing to morphing and energy harvesting. In order to employ the effective 33-mode of piezoelectricity, interdigitated electrodes have been used in the design of macro-fiber composites which employ piezoelectric fibers with rectangular cross section. In this article, we present an investigation of the two-way electroelastic coupling (in the sense of direct and converse piezoelectric effects) in bimorph cantilevers that employ interdigitated electrodes for 33-mode operation. A distributed-parameter electroelastic modeling framework is developed for the elastodynamic scenarios of piezoelectric power generation and dynamic actuation. Mixing rules (i.e. rule of mixtures) formulation is employed to evaluate the equivalent and homogenized properties of macro-fiber composite structures. The electroelastic and dielectric properties of a representative volume element (piezoelectric fiber and epoxy matrix) between two neighboring interdigitated electrodes are then coupled with the global electro-elastodynamics based on the Euler–Bernoulli kinematics accounting for two-way electromechanical coupling. Various macro-fiber composite bimorph cantilevers with different widths are tested for resonant dynamic actuation and power generation with resistive shunt damping. Excellent agreement is reported between the measured electroelastic frequency response and predictions of the analytical framework that bridges the continuum electro-elastodynamics and mixing rules formulation.

Keywords

Piezoelectric, energy harvesting, actuator, sensor, interdigitated electrodes, macro-fiber composites

Introduction

Piezoelectric materials are well suited for a variety of tasks since the piezoelectric effect is a reversible process in the form of the direct effect (conversion of mechanical strain to electric charge) and the converse effect (conversion of electric potential to mechanical strain). The most typical use of piezoelectric materials in bending is through the utilization of the "31-mode" with uniform electrodes. The use of 31-mode in bending has been well studied for sensing, energy harvesting, and static or dynamic actuation for decades (Baz and Ro, 1996; Dosch et al., 1992; Erturk, 2012; Erturk and Inman, 2009, 2011b; Hagood et al., 1990; Hagood and Von Flotow, 1991; Leadenham and Erturk, 2015a, 2015b; Leo, 2007; Smits and Choi, 1991), while the "33-mode" has been conventionally employed for longitudinal (axial) deformations through the use of piezoelectric stacks and bars (Cunefare et al., 2013; Feenstra et al., 2008; Shahab and Erturk, 2014a; Shahab et al., 2015a; Skow et al., 2014; Zhao and Erturk, 2014).

The concept of interdigitated electrodes (IDEs) with piezoelectric fibers was first introduced by Hagood et al. (1993) and Bent and Hagood (1997) since the 33-mode piezoelectric strain constant (50%–100% larger than that of the 31-mode) offered an intriguing design option to exploit inder bending deformation. The resulting active-fiber composite (AFC) structure was first characterized by Bent et al. (Bent, 1997; Bent et al.,

[1]Department of Biomedical Engineering and Mechanics, Virginia Polytechnic Institute and State University, Blacksburg, VA, USA
[2]George W. Woodruff School of Mechanical Engineering, Georgia Institute of Technology, Atlanta, GA, USA

Corresponding author:
Alper Erturk, George W. Woodruff School of Mechanical Engineering, Georgia Institute of Technology, Atlanta, GA 30332, USA.
Email: alper.erturk@me.gatech.edu

1995), and its properties were further investigated by others (Belloli et al., 2007; Berger et al., 2005; Brei and Cannon, 2004; Lin and Sodano, 2008, 2009) numerically and experimentally in next-generation efforts. However, the AFC technology employed piezoelectric fibers with circular cross section that limited the interactions between fibers and electrodes, yielding low electromechanical coupling and high dielectric loss. Solving this problem using fibers with rectangular cross section, researchers at the NASA Langley Research Center developed the macro-fiber composite (MFC) technology (High and Wilkie, 2003; Wilkie et al., 2000). The advantages of the MFC technology over monolithic piezoelectrics include increased flexibility, improved actuation authority, and anisotropic behavior. These characteristics of MFCs have led to experimental applications including structural sensing and vibration control (Browning et al., 2009; Sodano et al., 2004), bio-inspired locomotion (Cen and Erturk, 2013; Erturk and Delporte, 2011), acoustic wave devices (Collet et al., 2011; Matt and Di Scalea, 2007), morphing-wing and flapping-wing structures (Bilgen et al., 2010; Kim et al., 2007; Kim and Han, 2006; Paradies and Ciresa, 2009), and in-air/underwater dynamic actuation or energy harvesting (Cha et al., 2013, 2016; Erturk and Delporte, 2011; Shahab and Erturk, 2014b, 2014c, 2015a, 2015b; Shahab et al., 2015b).

It is worth mentioning that, other than their use in AFCs and MFCs, IDEs have also found use in micro-electro-mechanical systems (MEMS) as electrodes over monolithic electroelastic plates. IDEs are useful to MEMS since the 33-mode coupling allows for larger voltages to be produced in energy harvesting, overcoming the forward voltage requirements of diodes for DC rectification. Additionally, implementation of IDEs allows for an electrode surface only on one side of a piezoelectric material, simplifying the microfabrication process (Choi et al., 2006; Jeon et al., 2005). However, in the existing literature, modeling of the effect of 33-mode IDE actuators and harvesters in MEMS applications has been oversimplified or excluded completely.

In the early constitutive modeling efforts for 33-mode MFCs, Williams et al. (2002, 2004a, 2004b) presented an experimentally validated model for equivalent thermal expansion and mechanical properties of MFCs using modified classical mixing rules. Deraemaeker et al. (2009) reported the mixing rules-based calculations of the equivalent parameters and compared with manufacturer's data and experimental results. In another work, Deraemaeker and Nasser (2010) proposed a finite element method (periodic homogenization) to evaluate the equivalent properties of MFCs. More recently, Prasath and Arockiarajan (2015) presented analytical and numerical models to evaluate the effective thermo-electro-elastic properties of MFCs and the effect of thermal environment on the effective piezoelectric constants of MFCs. Most of these efforts have explored the constitutive behavior and structural homogenization alone. With increased applications on the dynamics of structures with MFCs, there is a growing need for coupling such homogenized constitutive modeling with a proper continuum electro-elastodynamics framework for energy harvesting, sensing, and actuation problems of both resonant and off-resonant applications.

In this article, building on the model presented by Deraemaeker et al. (2009), the electroelastic and dielectric properties of a representative volume element (RVE; piezoelectric fiber and epoxy matrix) between two subsequent IDEs are obtained using mixing rules, validated for a set of sample geometries, and then the RVE electroelastic mechanics is coupled with the global electroelastic dynamics based on the Euler–Bernoulli kinematics of MFC bimorphs following the analytical modeling approach of Erturk and Inman (2009). A linear distributed-parameter model for a bimorph assuming Euler–Bernoulli beam theory for energy harvesting and actuation is extended to the 33-mode and employed for parameter identification and model validation. The identified physical parameters of the MFC bimorphs are validated experimentally for different MFC types with the same overhang length but different active widths. The resulting framework that bridges mixing rules formulation with the continuum electro-elastodynamics is employed for energy harvesting and actuation problems.

Electroelastic equations of a bimorph cantilever with 33-mode piezoelectric coupling

Electroelastic properties of an MFC laminate using mixing rules formulation

An MFC laminate with IDE configuration is shown in Figure 1. The piezoelectric active material consists of lead zirconate titanate (PZT) fibers of rectangular cross section embedded in a Kapton film. As depicted in Figure 1(d), the strain axis and the electrical poling axis (the x-direction) are coincident. Therefore, the MFC laminate uses the 33-mode of piezoelectricity. Note that the manufacturer (Smart Material Corp.) uses polyester electrode sheets for waterproof behavior in custom-made samples investigated in this work (however, the resulting properties are similar to those of the standard samples).

The non-uniform electric field lines (Beckert and Kreher, 2003; Bowen et al., 2006; Deraemaeker et al., 2009) (curvature of the lines is highly dependent on the distance between the electrodes) through the piezoelectric fibers and dead zones are depicted in Figure 1(b). Because of the non-uniform electric field and heterogeneous complex structure involving active and passive regions (in Figure 1(b); PZT fiber and epoxy,

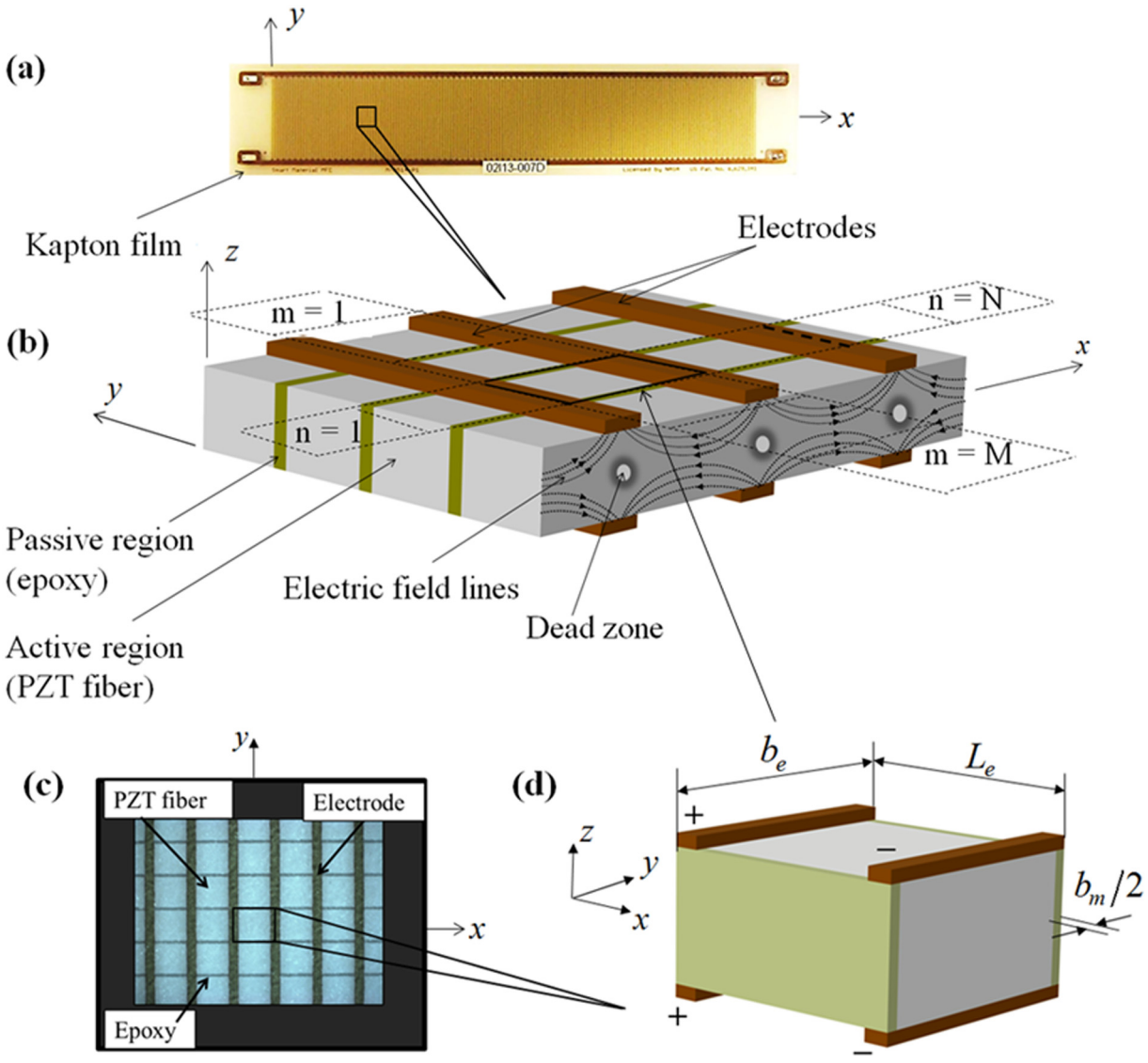

Figure 1. (a) An MFC laminate using the 33-mode of piezoelectricity; (b) volumetric representation of an MFC showing PZT fibers with electric field lines, polymer matrix (epoxy), and interdigitated electrodes; (c) digital image of the planar surface of an MFC actuator (M8514-P1 with polyester electrode sheets and approximately 90% volume fraction of PZT fibers) under optical microscope; and (d) an RVE (in symmetric shape).

respectively) in MFCs, a straightforward analytical integration using standard PZT properties cannot be performed to obtain the electromechanical coupling and capacitance parameters. In this work, mixing rules formulation is employed to evaluate the equivalent and homogenous properties of MFCs from the constitute properties. To this end, the piezoelectric fiber segments between subsequent IDEs are modeled as a set of piezoelectric elements in 33-mode and they are combined in parallel. That is, in Figure 1, each RVE is a capacitor which is connected in parallel to the remaining RVEs along the length and width of the MFC laminate.

The linear constitutive equations for a piezoelectric thin beam (RVE in Figure 1(d)) with 33-mode coupling are as follows (Erturk and Inman, 2011b)

$$T_3 = c^E_{33,e} S_3 - e_{33,e} E_3 \tag{1}$$

$$D_3 = e_{33,e} S_3 + \varepsilon^S_{33,e} E_3 \tag{2}$$

where T_3 is the stress, S_3 is the strain, E_3 is the electric field, D_3 is the electric displacement, $c^E_{33,e}$ is the elastic modulus at constant electric field, $e_{33,e}$ is the effective piezoelectric stress constant, $\varepsilon^S_{33,e}$ is the permittivity component at constant strain, and subscript e stands for the equivalent properties.

The equivalent elastic modulus ($c^E_{33,e}$), piezoelectric charge constant ($d_{33,e}$), and permittivity constant ($\varepsilon^S_{33,e}$) are defined based on mixing rules formulation for an RVE in Figure 1(d) (Agarwal et al., 2006; Deraemaeker et al., 2009)

$$c^E_{33,e} = \nu c^E_{33,p} + (1-\nu)c^E_{33,m} \tag{3}$$

$$d_{33,e} = \left(\frac{1}{c^E_{33,e}}\right)\nu d_{33,p}c^E_{33,p} \tag{4}$$

$$\varepsilon^S_{33,e} = \left[\nu\varepsilon^T_{33,p} + (1-\nu)\varepsilon^T_{33,m}\right] - d^2_{33,e}c^E_{33,e} \tag{5}$$

where ν is the PZT fiber volume fraction and is obtained by the measurement done from the digital image of the planar surface of an MFC actuator (shown in Figure 1(c)) and ε^T_{33} is the permittivity component at constant stress. The subscripts p and m stand for PZT fiber and matrix (epoxy) properties of RVE, respectively. The mixing rules-based effective electroelastic parameters will be coupled with the electroelastic dynamics based on the Euler–Bernoulli kinematics in the next section to obtain the global parameters (e.g. capacitance and electromechanical coupling) of an MFC bimorph and to exploit the 33-mode of piezoelectricity in bending mode. The analysis of an Euler–Bernoulli bimorph beam with monolithic piezoelectric layers in 31-mode has been thoroughly covered in previous work (Erturk and Inman, 2009) for energy harvesting applications. The key concepts for 33-mode use will be developed next and applied to experimental problems of actuation and energy harvesting in this article.

Coupled mechanical equation under base excitation

Schematics of MFC bimorph cantilevers for dynamic actuation with fixed base and energy harvesting from base motion are shown in Figure 2. Each symmetric bimorph is composed of two MFC laminates (Figure 1(a)) which are combined in a vacuum bonding process using high-shear-strength epoxy (this process is described elsewhere (Anton et al., 2010)). Therefore, the bimorphs contain a bonding layer in addition to the MFC laminates.

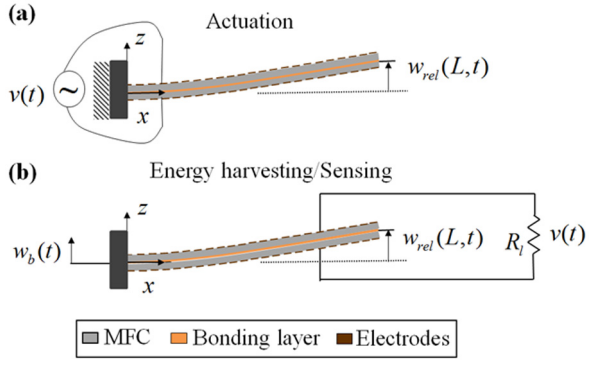

Figure 2. Schematic of a cantilevered MFC bimorph composed of two bonded single-layer MFC laminates: (a) dynamic actuation and (b) transverse base excitation.

The MFC bimorph cantilever configurations shown in Figure 2 are modeled here based on the Euler–Bernoulli beam theory since length/thickness ratio is very high. Deformations are assumed to be small and the composite structure is assumed to exhibit linear material behavior. The partial differential equation governing the base-excited cantilevered bimorph is as follows (voltage actuation case will be addressed briefly later on)

$$-\frac{\partial^2 M(x,t)}{\partial x^2} + c_\alpha \frac{\partial^5 w_{rel}(x,t)}{\partial x^4 \partial t} + c_\beta \frac{\partial w_{rel}(x,t)}{\partial t} + m_s \frac{\partial^2 w_{rel}(x,t)}{\partial t^2} = -m_s \frac{\partial^2 w_b(t)}{\partial t^2} \tag{6}$$

where $w_{rel}(x,t)$ is the transverse displacement of the reference surface relative to its base at position x and time t, c_α is the stiffness-proportional damping coefficient, c_β is the mass-proportional damping coefficient, m_s is the mass per unit length of the beam, $M(x,t)$ is the internal bending moment, and $w_b(t)$ is the transverse base displacement.

The internal bending term in equation (6) is the first moment of the axial stress field over the cross section of MFC laminate

$$M(x,t) = \int_A T_3 z dA = \sum_{m=1}^{M} b_e \left(\int_{-h_{\bar{p}}-h_b/2}^{-h_b/2} T_3 z dz + \int_{h_b/2}^{h_{\bar{p}}+h_b/2} T_3 z dz \right) \tag{7}$$

where, in each RVE (Figure 1(d)), b_e is the sum of the width of piezoelectric fiber and is the width of the matrix layer (epoxy) in the direction of bimorph width. In equation (7), M is the number of RVEs in active width of the bimorph (b); therefore, $b = Mb_e$. Furthermore, $h_{\bar{p}}$ is the thickness of the piezoelectric fiber, h_b is the thickness of the bonding and Kapton layers, and T_3 is the previously defined stress component (in the x-direction) given by equation (1). The stress component for bonding (epoxy) and Kapton layers are assumed to be negligible as their stiffness is much less than the stiffness of PZT fibers (considering also that the bonding layer is at the neutral surface level). The electric field in equation (1) can be given in terms of the voltage across the electrodes, $v(t)$. The voltage across the terminals of each MFC laminate is $v(t)/2$ when two MFC laminates are connected in series and $v(t)$ when connected in parallel. The electric field is defined as $E_3 = \pm v(t)/L_e$, where L_e is the distance between two subsequent electrode fingers (shown in Figure 1(d)). The plus and minus difference is a result of the difference in poling of the piezoelectric material which is an important parameter for the series or parallel connection of the piezoelectric layers as in the case

of 31-mode bimorphs as well (Erturk and Inman, 2011b). In Figure 1(c), each RVE is essentially a capacitor which is linked in parallel to the adjacent RVEs along the length and width of the MFC laminate. Furthermore, the piezoelectric stress constant $e_{33,e}$ in equation (1) can be given in terms of more common piezoelectric strain constant $d_{33,e}$ as $e_{33,e} = d_{33,e}c^E_{33,e}$. The axial strain at a certain level (z) from the neutral axis of the symmetric composite beam is simply proportional to the curvature of the beam at position x

$$S_3(x,z,t) = -z\frac{\partial^2 w_{rel}(x,t)}{\partial x^2} \tag{8}$$

Substituting equation (1) into equation (7) and multiplying the electrical term by $[H(x-(n-1)L_e) - H(x-nL_e)]$, the internal bending moment at the axial position x and time t becomes

$$M^s(x,t) = -D\frac{\partial^2 w_{rel}(x,t)}{\partial x^2} + \sum_{n=1}^{N} \vartheta_s v(t)[H(x-(n-1)L_e) - H(x-nL_e)] \tag{9}$$

$$M^p(x,t) = -D\frac{\partial^2 w_{rel}(x,t)}{\partial x^2} + \sum_{n=1}^{N} \vartheta_p v(t)[H(x-(n-1)L_e) - H(x-nL_e)] \tag{10}$$

where D is the bending stiffness of the composite cross section, $H(x)$ is the Heaviside function, and n is the index of the RVE at a distance x from the fixed end of the bimorph. Note that, here and hereafter, the subscripts and superscripts s and p, respectively, stand for the series and parallel connections of MFC laminates. In equations (9) and (10), N is the number of RVEs in the active overhang length, L, as $L = NL_e$. The backward coupling terms for the series and parallel connection cases (ϑ_s and ϑ_p, respectively) can be expressed as follows:

$$\vartheta_s = \sum_{m=1}^{M} \frac{e_{33}b_e}{2h_{\tilde{p}}}\left[\left(h_{\tilde{p}} + \frac{h_b}{2}\right)^2 - \frac{h_b^2}{4}\right] = \sum_{m=1}^{M} \frac{e_{33}b_e h_{\tilde{p}}}{2L_e}(h_{\tilde{p}} + h_b) = Md_{33,e}c^E_{33,e}\frac{A_e}{L_e}h_{pc} \tag{11}$$

$$\vartheta_p = 2\vartheta_s = 2Md_{33,e}c^E_{33,e}\frac{A_e}{L_e}h_{pc} \tag{12}$$

For each RVE, A_e is the effective cross-sectional area and h_{pc} is the position of center of piezoelectric fibers from the neutral axis (in thickness direction). The governing mechanical equation with electromechanical coupling can be obtained using equation (9) or (10) in equation (6). For instance, for the parallel connection of MFC laminates, the electromechanically coupled beam equation can be obtained as follows

$$D\frac{\partial^4 w_{rel}(x,t)}{\partial x^4} + c_\alpha\frac{\partial^5 w_{rel}(x,t)}{\partial x^4 \partial t} + c_\beta\frac{\partial w_{rel}(x,t)}{\partial t} + m_s\frac{\partial^2 w_{rel}(x,t)}{\partial t^2} - \vartheta_p v(t)\left[\frac{d\delta(x)}{dx} - \frac{d\delta(x-L)}{dx}\right] = -m_s\frac{\partial^2 w_b(t)}{\partial t^2} \tag{13}$$

Likewise, for the series connection case, ϑ_s is used for the backward coupling term in equation (13).

Coupled electrical circuit equation

The electric current output is obtained from the integral form of Gauss's law as follows

$$\frac{d}{dt}\left(\int_A \mathbf{D}\cdot\mathbf{n}\,dA\right) = \frac{v(t)}{R_l} \tag{14}$$

where $\mathbf{D}$ is the vector of electric displacement components, $\mathbf{n}$ is the unit outward normal, and the integration is performed over the effective cross section of the MFC laminate, A, where $A \cong MA_e$. The inner product of the integrand in equation (14) is obtained using the electric displacement D_3 given in equation (2). Using equation (8) (with $z = h_{pc}$) for the average bending strain in terms of the curvature and the electric field in terms of the voltage across the electrodes ($E_3 = -v(t)/L_e$), equation (14) yields

$$C_p\frac{dv(t)}{dt} + \frac{v(t)}{R_l} + Md_{33,e}c^E_{33,e}\frac{A_e}{L_e}h_{pc}\int_0^L \frac{\partial^3 w_{rel}(x,t)}{\partial x^2 \partial t}dx = 0 \tag{15}$$

where the internal capacitance is

$$C_p = \sum_{m=1}^{M}\sum_{n=1}^{N} \varepsilon^S_{33,e}\frac{A_e}{L_e} = MN\varepsilon^S_{33,e}\frac{A_e}{L_e} \tag{16}$$

Modal analysis of mechanical base excitation and electrical actuation problems

The transverse deflection of the reference surface (relative to the clamped end) at position x and time t is given by

$$w_{rel}(x,t) = \sum_{r=1}^{\infty} \phi_r(x)\eta_r(t) \tag{17}$$

where $\phi_r(x)$ and $\eta_r(t)$ are the mass-normalized eigenfunction and the generalized modal coordinate for the rth mode, respectively. The eigenfunctions denoted by

$\phi_r(x)$ can be obtained for the transverse vibration of a uniform clamped-free beam as

$$\phi_r(x) = \sqrt{\frac{1}{m_s L}}\left[\cos\frac{\lambda_r}{L}x - \cosh\frac{\lambda_r}{L}x + \frac{\sin\lambda_r - \sinh\lambda_r}{\cos\lambda_r + \cosh\lambda_r}\left(\sin\frac{\lambda_r}{L}x - \sinh\frac{\lambda_r}{L}x\right)\right] \quad (18)$$

where λ_r is the eigenvalue of the rth mode obtained from the characteristic equation given by

$$1 + \cos\lambda\cosh\lambda = 0 \quad (19)$$

The expression given for $\phi_r(x)$ satisfies the companion orthogonality conditions (Erturk and Inman, 2009, 2011b)

$$\int_0^L \phi_s(x) m_s \phi_r(x) dx = \delta_{rs} \quad (20)$$

$$\int_0^L \phi_s(x) D \frac{d^4\phi_r(x)}{dx^4} dx = \omega_r^2 \delta_{rs} \quad (21)$$

where $\omega_r = \lambda_r^2\sqrt{D/m_s L^4}$ is the undamped short-circuit natural frequency of the rth vibration mode and δ_{rs} is the Kronecker delta.

The base displacement is assumed to be harmonic of the form $w_b(t) = W_0 e^{j\omega t}$ (where ω is the excitation frequency and j is the unit imaginary number). The modal forcing is expressed as $f_r(t) = F_r e^{j\omega t}$ where the amplitude F_r is

$$F_r = -\sigma_r \omega^2 W_0 \quad (22)$$

where

$$\sigma_r = -m_s \int_0^L \phi_r(x) dx \quad (23)$$

Then assuming harmonic steady-state modal mechanical response and voltage response of the forms $\eta_r(t) = H_r e^{j\omega t}$ and $v(t) = V e^{j\omega t}$, and using equation (17) in equations (13) and (15) in conjunction with the orthogonality conditions yield the electromechanically coupled linear equations for the complex amplitudes

$$(\omega_r^2 - \omega^2 + j2\zeta_r\omega_r\omega)H_r - \theta_r V = F_r \quad (24)$$

$$\left(\frac{1}{R_l} + j\omega C^{eq}\right)V + j\omega\sum_{r=1}^{\infty}\theta_r H_r = 0 \quad (25)$$

where θ_r is the modal electromechanical coupling, ζ_r is the modal mechanical damping ratio, and C^{eq} is the equivalent capacitance. The modal electromechanical coupling and equivalent capacitance depend on the way the MFC laminates are connected. The analytical expressions for the equivalent capacitance and modal electromechanical coupling are given in Table 1 for the series and parallel connections of the individual MFC laminates, similar to the case of the 31-mode problem with uniform electrodes (Erturk and Inman, 2011b).

Table 1. Modal electromechanical coupling and equivalent capacitance of an MFC bimorph for the series and parallel connections of the MFC laminates.

	Series connection	Parallel connection
θ_r	$Md_{33,e}c^E_{33,e}\frac{A_e}{L_e}h_{pc}\frac{d\phi_r(x)}{dx}\Big\|_{x=L}$	$2Md_{33,e}c^E_{33,e}\frac{A_e}{L_e}h_{pc}\frac{d\phi_r(x)}{dx}\Big\|_{x=L}$
C^{eq}	$MN\bar{e}^S_{33,e}\frac{A_e}{2L_e}$	$2MN\bar{e}^S_{33,e}\frac{A_e}{L_e}$

MFC: macro-fiber composite.

The actuation problem can be represented in a similar fashion such that the excitation is due to the harmonic voltage input and there is no base excitation ($F_r = 0$), yielding

$$(\omega_r^2 - \omega^2 + j2\zeta_r\omega_r\omega)H_r = \theta_r V \quad (26)$$

$$-I + j\omega V C^{eq} + j\omega\sum_{r=1}^{\infty}\theta_r H_r = 0 \quad (27)$$

Here, as compared to equation (25), V/R_l is replaced with $-i(t) = -Ie^{j\omega t}$, where $i(t)$ is the electric current input (negative sign indicates current flow into the system).

Energy harvesting from base excitation: voltage output and tip velocity frequency response functions

Closed-form solutions for the voltage and vibration response, $v(t)$ and $w_{rel}(x,t)$, can be obtained from equations (24) and (25) for steady-state behavior. The frequency-domain transfer functions, that is, frequency response functions (FRFs), are extracted as (Erturk and Inman, 2009, 2011b)

$$\alpha(\omega) = \frac{v(t)}{-\omega^2 W_0 e^{j\omega t}} = \frac{\sum_{r=1}^{\infty}[(-j\omega\theta_r\sigma_r)/(\omega_r^2 - \omega^2 + j2\zeta_r\omega_r\omega)]}{(1/R_l) + j\omega C^{eq} + \sum_{r=1}^{\infty}[(j\omega\theta_r^2)/(\omega_r^2 - \omega^2 + j2\zeta_r\omega_r\omega)]} \quad (28)$$

$$\beta(\omega,x) = \frac{w_{rel}(x,t)}{-\omega^2 W_0 e^{j\omega t}} = \sum_{r=1}^{\infty}\frac{[\sigma_r + \theta_r\alpha(\omega)]\phi_r(x)}{\omega_r^2 - \omega^2 + j2\zeta_r\omega_r\omega} \quad (29)$$

Finally, the displacement FRF relative to the fixed end can be modified to express the absolute velocity response, $\gamma(\omega,x)$, to conveniently compare model simulations with experimental measurements

$$\gamma(\omega,x) = \frac{w_b(t) + w_{rel}(x,t)}{\ddot{w}_b(t)} = \frac{1}{j\omega} + j\omega\beta(\omega,x) \quad (30)$$

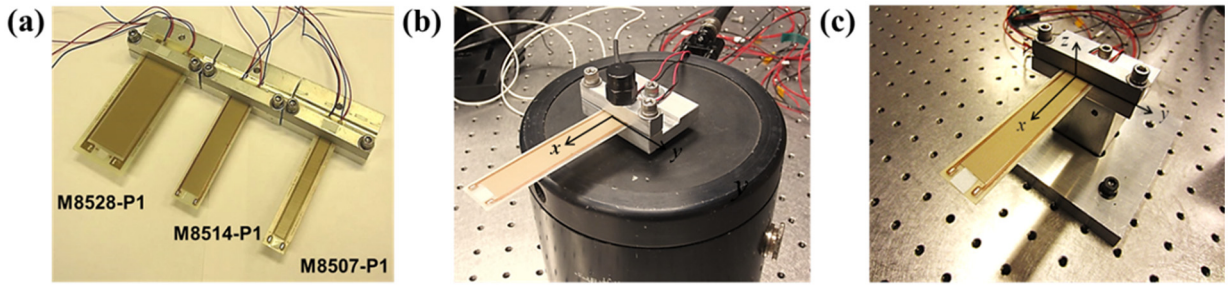

Figure 3. (a) Cantilevered MFC bimorph samples in aluminum clamps; (b) close-up view of an M8514-P1 type bimorph cantilever mounted on electromechanical shaker with an accelerometer; and (c) dynamic actuation test for sample bimorph (M8514-P1) cantilever in fixture mounted rigidly to table.

Dynamic actuation: tip velocity and admittance FRFs

Solving equations (26) and (27) at steady state yields the displacement FRF, $\chi(\omega, x)$, and the admittance FRF, $\varphi(\omega)$

$$\chi(\omega, x) = \frac{w_{rel}(x,t)}{Ve^{j\omega t}} = \sum_{r=1}^{\infty} \frac{\theta_r \phi_r(x)}{\omega_r^2 - \omega^2 + 2j\zeta_r \omega_r \omega} \tag{31}$$

$$\varphi(\omega) = \frac{i(t)}{v(t)} = \frac{I}{V} = j\omega \left(C^{eq} + \sum_{r=1}^{\infty} \frac{\theta_r^2}{\omega_r^2 - \omega^2 + 2j\zeta_r \omega_r \omega} \right) \tag{32}$$

For experimental comparisons, the tip velocity FRF is obtained simply from $j\omega\chi(\omega, x)$.

Experimental validations for energy harvesting and dynamic actuation

For experimental validation of the energy harvesting and actuation models presented in the previous section, three cantilevered MFC bimorphs were tested focusing on the fundamental mode of bending vibration. The MFCs, fabricated by Smart Material Corp., have active length of 85 mm (region containing piezoelectric fibers) for all samples in unclamped condition. Each bimorph is made from two identical MFC laminates labeled as M8507-P1, M8514-P1, and M8528-P1 (Figure 3(a)) with active widths of 7, 14, and 28 mm, respectively.

The individual MFC laminates were processed with a vacuum bonding system to create symmetric bimorphs which are then cantilevered in aluminum clamps as shown in Figure 3(a). The overhang lengths of the MFC bimorphs are approximately 75.5 mm, while the total thicknesses are around 0.61 mm. The electrode leads of the MFC bimorphs are connected in parallel throughout the experiments discussed in this article and the focus is placed on the energy harvesting and dynamic actuation problems for the fundamental bending vibration mode with geometrically and materially linear behavior. Energy harvesting experiments (Figure 3(b)) were conducted through a Spectral Dynamics SigLab data acquisition device that received base acceleration data (using a Kistler accelerometer with a Kistler Signal Conditioner), absolute velocity data measured at the tip of the bimorph by means of a laser Doppler vibrometer (Polytec PDV 100), and voltage across the resistive load (IET decade box) for a set of resistance values. Sinusoidal excitation with 10 averages was fed to a B&K electromechanical shaker through an HP power amplifier for base excitation over a range of frequencies centered around the first mode. Actuation experiments (Figure 3(c)) were conducted in the same setup, but with a fixed mount instead of a shaker and a high voltage amplifier (Trek, Inc. Model 2220) which provides reference voltage and monitors current drawn during the actuation process.

System parameters by experimental identification and model simulation

The geometric properties for the active (PZT fibers) and passive (epoxy, electrodes, and Kapton film) layers of MFCs are shown in Figure 4 for both xz-plane and yz-plane (cross section). From the surface image (e.g. Figure 1(c) for M8514-P1 bimorph), the width of each piezoelectric fiber is approximately 355.5 μm and each epoxy layer between the fibers has a width of 34.4 μm. Since the total active width is 14 mm, this sample (M8514-P1) has approximately 36 piezoelectric fibers (i.e. $M = 36$) and the volume fraction is $\nu = 0.9$. The average spacing between two subsequent electrodes is 407.18 μm. Therefore, the number of RVEs over the beam length is 185 ($N = 185$). After measuring the capacitance of the MFCs and using equation (16), the average effective surface area of each RVE, A_e, is calculated as 0.02 mm^2, while h_{pc} (distance from the reference surface, i.e. neutral axis level, to fiber center in the thickness direction) is 157 μm. The MFCs use Navy II type piezoelectric ceramic for which the effective value of the piezoelectric constant for an RVE is $e_{33,e} = 19.1\,\mathrm{C/m^2}$. In Table 2, the properties of PZT fibers, epoxy, RVE (the equivalent properties for an RVE are calculated by mixing rules), and those of the overall MFC are given.

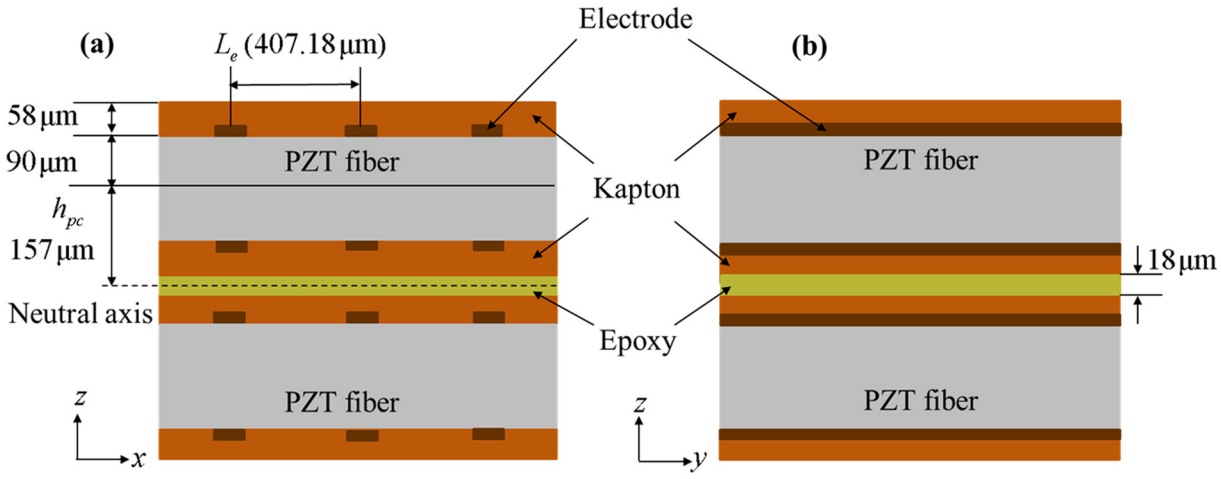

Figure 4. Two-dimensional representation of an MFC bimorph (made from two identical MFC laminates bonded using high-shear-strength epoxy with electrodes (epoxy and copper fibers) perpendicular to the PZT fibers embedded in Kapton film). (a) Geometric parameters in the *xz*-plane and (b) sequence of layers in the cross-sectional area (*yz*-plane: not to scale). Approximate data provided by manufacturer or measured under optical microscope.

Table 2. Properties of the active layer (PZT fiber), passive layer or matrix (epoxy), RVE, and the 33-mode MFCs using analytical mixing rules ($\varepsilon_{33}^S = \varepsilon_{33}^T - d_{33}^2 c_{33}^E$ and $\varepsilon_0 = 8.854\,\text{pF/m}$).

	PZT fiber	Epoxy	RVE	MFC
c_{33}^E, c_{33} (GPa)	48.30	3.10	43.78	31.10
d_{33} (pm/V)	440	–	437	437
$\varepsilon_{33}^T/\varepsilon_0$	1850	4.25	1665	1665
ε_{33}^S (nF/m)	7.02	–	6.38	8.80

PZT: lead zirconate titanate; RVE: representative volume element; MFC: macro-fiber composite.

Table 3. Identified parameters from dynamic actuation and energy harvesting experiments for the fundamental bending mode.

	M8507-P1	M8514-P1	M8528-P1
f_{sc} (Hz)	44.6	47.9	46.4
f_{oc} (Hz)	46.1	48.5	47.2
ζ (%)	1.8	2	1.5
θ (10^{-3} C/m$\sqrt{\text{kg}}$)	3.5	4.5	9
C^{eq} (nF)	3.8	5.5	17.5

Note that the electrode layers are made from epoxy and copper fibers (volume fraction of copper is approximately 24%) which are perpendicular to the PZT fibers, and the composite structure is embedded in Kapton film. The in-plane (*yz*-plane) sequence of layers for a MFC is shown in detail in Figure 4(b). The equivalent properties of electrode–Kapton layer are calculated using mixing rules formulation. Then, the properties of an MFC are calculated from the properties of all the included layers (PZT–epoxy (RVE in Figure 1(d)) and electrode–Kapton layers). For example, the RVE has the equivalent elastic modulus of 48.3 GPa, and by including the electrode and Kapton layers (elastic modulus is 117.2 and 2.8 GPa for copper and Kapton, respectively), the overall c_{33}^E is evaluated as 31.1 GPa and the piezoelectric constant is $e_{33} = 13.6\,\text{C/m}^2$ for the MFC. The reported values in Table 2 compare favorably with previously published numerical and experimental data (Deraemaeker et al., 2009) as well as with data from the manufacturer's datasheet.

Having mixing rules-based equivalent and homogenized properties, the modal electromechanical coupling (θ) for the bimorph MFC (with parallel connection of the laminates) is obtained from Table 1 for fundamental bending vibration mode ($r = 1$). For each cantilevered bimorph MFC sample, the short-circuit resonance frequency, the mechanical damping ratio, and the equivalent capacitance are obtained and shown in Table 3. Note that the modal electromechanical coupling is related to the difference between the short- and open-circuit natural frequencies (Erturk and Inman, 2011a) (i.e. knowing the short- and open-circuit natural frequencies and the capacitance, the modal electromechanical coupling can be calculated).

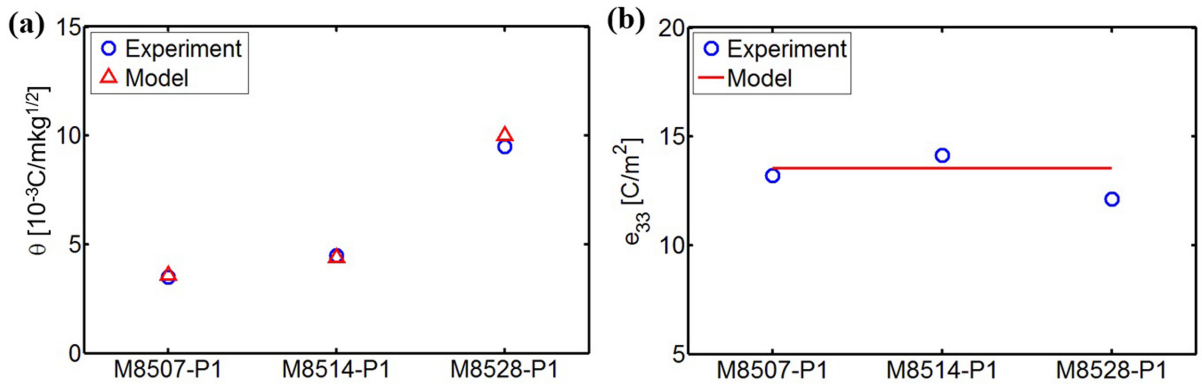

Figure 5. Experimental and analytical results for (a) modal electromechanical coupling and (b) equivalent piezoelectric stress constant for all samples.

In order to demonstrate the consistency of model predictions and experimentally identified parameters, Figure 5 shows the modal electromechanical coupling and the piezoelectric stress constant for all three samples. It is worth adding that various sources of uncertainly exist due to manufacturing imperfections (both in MFC fabrication and in their bonding process to obtain a bimorph). Note that the modal coupling term increases with increasing sample width (Figure 5(a)) and roughly the same piezoelectric constant is obtained for each sample (Figure 5(b)) using the coupling term in its expression (Table 1). Next, the results from the mixing rules formulation of the effective electroelastic, elastic, and dielectric properties of MFCs can be fully bridged with the global electroelastic dynamics of MFC bimorphs for energy harvesting and actuation.

Energy harvesting from base excitation: mechanical excitation

Figure 6(a) to (c) shows the voltage output and tip velocity FRFs obtained from equations (28) and (30) for M8507-P1, M8514-P1, and M8528-P1 bimorphs using the energy harvesting setup (Figure 3(b)). The denominator of these FRFs is normalized with respect to gravitational acceleration (g). The tests were conducted at low base excitation levels around the fundamental resonance frequency for a set of resistive electrical loads ranging from 100 Ω to ~9.09 MΩ (more precisely the resistor set is [0.1 1 10 99 909.1 5000 9082.6] kΩ). As the load resistance is increased, the resonance frequency shifts from the short-circuit resonance frequency to the open-circuit resonance frequency. It is observed that, by changing the load resistance from short- to open-circuit conditions, the voltage output increases uniformly and the resonance frequency for moderate resistive loads takes a value between the short- and open-circuit resonance frequencies as expected from basic energy harvester dynamics. With increased load resistance, the peak vibration amplitude decreases considerably from the peak of short-circuit condition to a certain value and then it is amplified at the open-circuit resonance frequency. This phenomenon results from the changing electrical loading condition of the bimorph and shunt damping effect due to Joule heating in the resistor (Lesieutre, 1998; Lesieutre et al., 2004).

The voltage, electric current, power output, and the tip velocity (per base acceleration) versus load resistance graphs for excitations at the fundamental short- and open-circuit resonance frequencies (44.6 and 46.1 Hz, respectively) are shown in Figure 7(a) to (d) for M8507-P1. For brevity, the remaining samples are not graphically presented here as the overall trends and model versus experiment agreement qualities are similar. It is observed from Figure 7(a) and (b) that the voltage amplitude and the current amplitude versus load resistance have the opposite monotonic trends. That is, as the load resistance increases, the voltage output increases and the current output decreases monotonically. The voltage for excitation at the short-circuit resonance frequencies is higher when the system (i.e. the electrical loading condition) is close to short-circuit conditions, and vice versa. For the 0.74 MΩ load resistance, both excitation frequencies yield approximately the same voltage amplitude (49.1 V/g). The electrical power output versus load resistance graph for excitations at the fundamental short- and open- circuit resonance frequencies is plotted in Figure 7(c). Since it is a product of two variables with opposite trends (i.e. voltage and current given in Figure 7(a) and (b)), the power output exhibits peak values for certain load resistance values. Since the system is lightly damped and strongly coupled (Erturk and Inman, 2011b) approximately, the same power output (4.6 mW/g^2) is delivered to substantially different optimal resistance values for excitations at 44.6 and 46.1 Hz. Figure 7(d) shows that the vibration amplitude at the fundamental short- and open-circuit resonance frequencies is attenuated significantly for the optimum electrical load of the

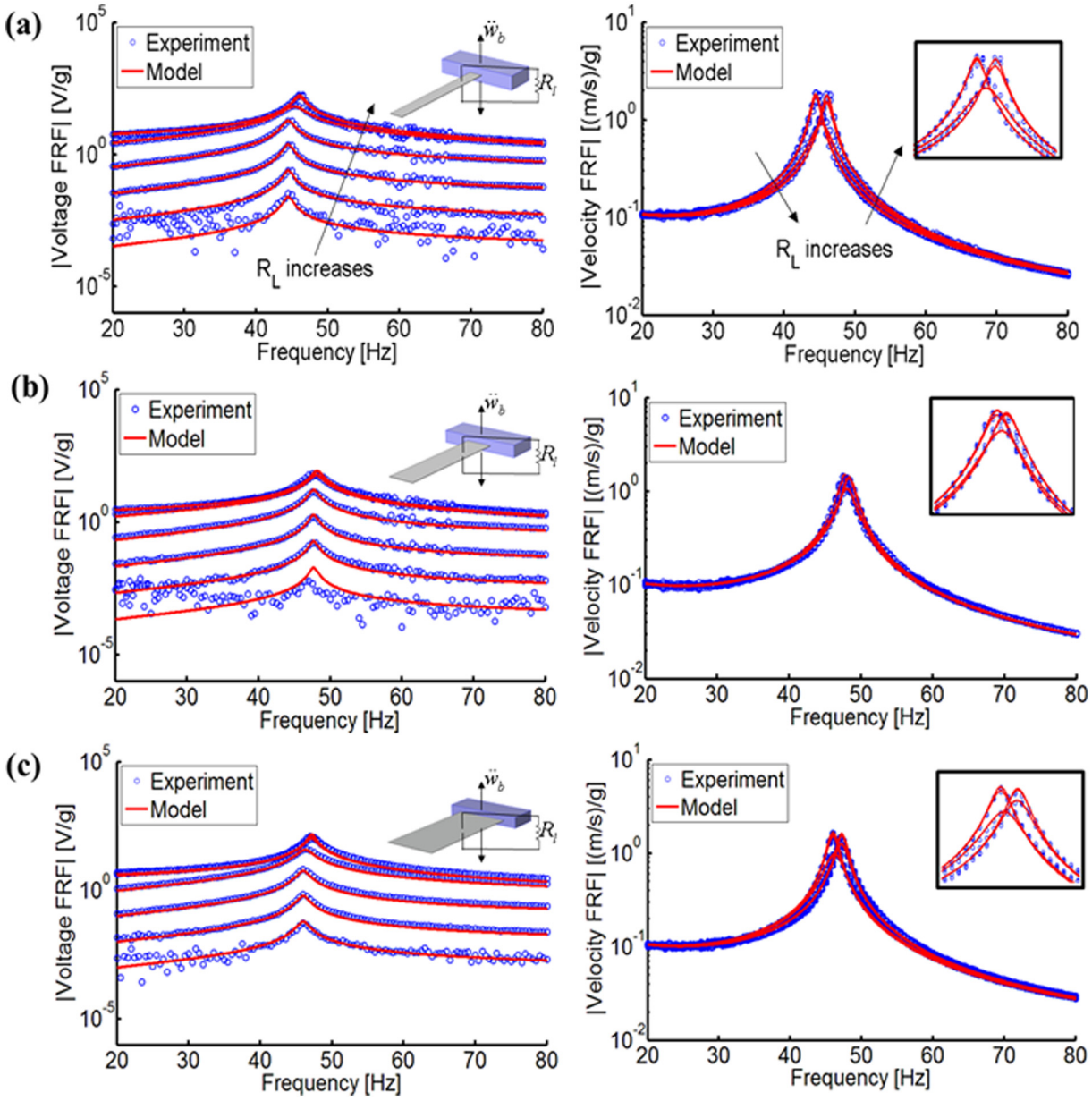

Figure 6. Experimental and analytical frequency response results for energy harvesting from base excitation for a set of resistive loads: voltage output FRFs (left) and tip velocity FRFs (right) for a set of resistors for (a) M8507-P1; (b) M8514-P1; and (c) M8528-P1.

maximum power output (cf. Figure 7(c)) as a result of the previously mentioned Joule heating effect associated with resistive shunting. Note that the nonlinear effects can easily be pronounced under higher base excitation levels and a proper nonlinear nonconservative modeling framework (Leadenham and Erturk, 2015b; Stanton et al., 2010; Usher and Sim, 2005; Wolf and Gottlieb, 2002) is required for such cases.

Dynamic actuation: electrical excitation

Finally, the same modeling framework is employed to predict the electromechanical response in the case of dynamic actuation around the fundamental resonance frequency for the same set of system parameters. The setup used in dynamic actuation experiments was previously shown in Figure 3(c). In typical applications, the admittance FRF (how much current is drawn for unit actuation voltage input) is useful to quantify actuation power consumption while the tip velocity FRF (structural response for unit actuation voltage input) is typically the main interest. For low actuation voltage levels (to obtain geometrically and materially linear behavior), the admittance and tip velocity FRFs of the three bimorphs (M8507-P1, M8514-P1, and M8528-P1) are shown in Figure 8. The model predictions using equations (31) and (32) exhibit excellent agreement with the experimental frequency response data, confirming the

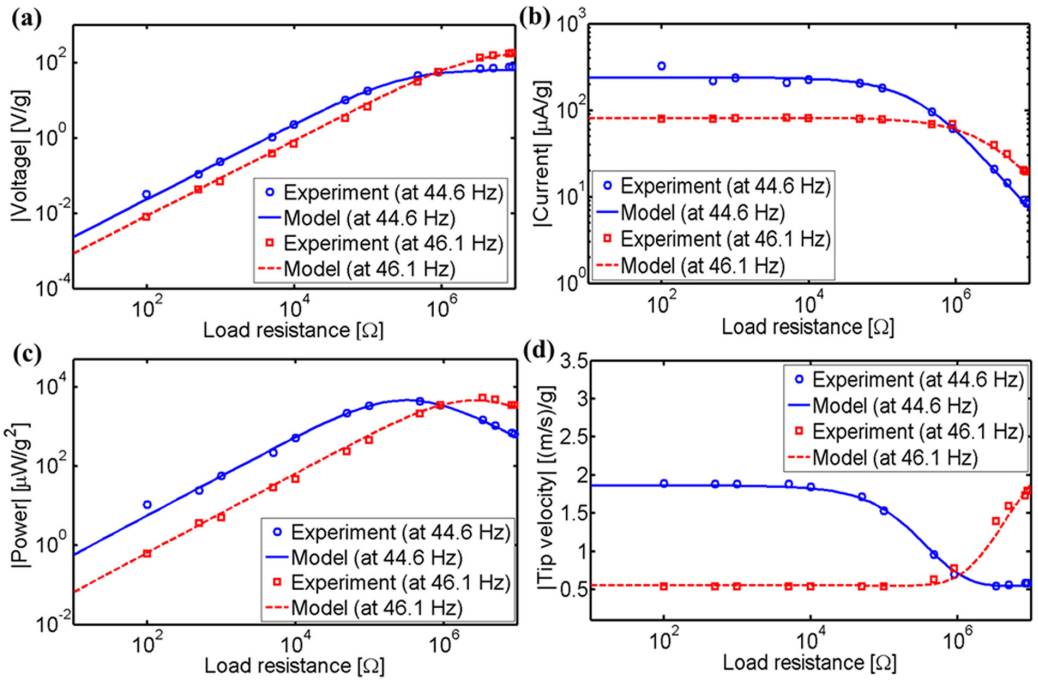

Figure 7. (a) Voltage, (b) current, (c) power, and (d) tip velocity amplitude (per base acceleration input) versus load resistance for excitations at fundamental short- and open-circuit resonance frequencies.

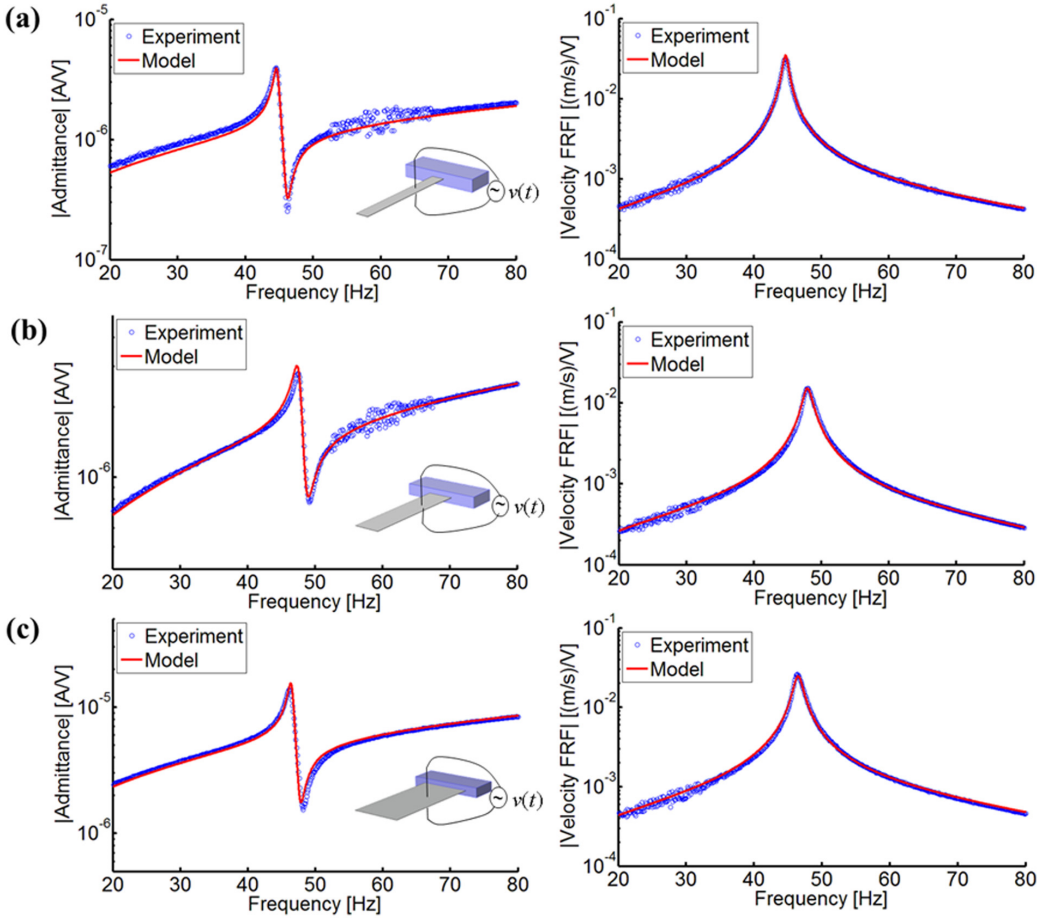

Figure 8. Experimental and analytical frequency response results for dynamic actuation: admittance FRF (left) and tip velocity FRF (right) for (a) M8507-P1; (b) M8514-P1; and (c) M8528-P1.

validity of the framework with two-way coupling given in this article. Once again, under higher excitation levels, nonlinear effects would be pronounced and such effects are not accounted for in the present effort. It is worth mentioning that while nonlinear dynamics of 31-mode bimorphs with uniform electrodes were studied in the existing literature (Leadenham and Erturk, 2015b; Stanton et al., 2010; Usher and Sim, 2005; Wolf and Gottlieb, 2002), there is a need for similar efforts for MFCs with moderate to large fields (mechanical/electrical) and geometric deformations.

Conclusion

An experimentally validated electro-elastodynamic modeling framework was developed for energy harvesting, sensing, and actuation applications of 33-mode MFC bimorph cantilevers with IDEs. Homogenized electromechanical constitutive properties of MFCs were obtained based on the mixing rules formulation and then coupled with the distributed-parameter electroelastic model to give the global electroelastic parameters of MFCs with different aspect ratios. Experimentally validated equivalent analytical expressions for the capacitance and modal electromechanical coupling terms were given for the series and parallel connections of MFC laminates. The analytical modal electromechanical coupling terms were shown to depend directly on the width of the sample, yielding identical piezoelectric constants when normalized with respect to width. This was confirmed for a set of MFC bimorph samples with different widths via carefully conducted tests. Experiments were performed for energy harvesting from base excitation (as a mechanical excitation problem) and dynamic actuation (as an electrical excitation problem) around resonance. Experimentally obtained electromechanical frequency response curves were successfully predicted using the analytical framework given in this paper. This successful modeling framework connects mixing rules formulation with the continuum homogenized electroelastic dynamics to exploit in a variety of applications of MFCs ranging from vibration energy harvesting and biomimetic locomotion to structural sensing and vibration control. Future work will focus on geometric and material nonlinearities under moderate to high mechanical and electrical excitation levels.

Declaration of Conflicting Interests

The author(s) declared no potential conflicts of interest with respect to the research, authorship, and/or publication of this article.

Funding

The author(s) disclosed receipt of the following financial support for the research, authorship, and/or publication of this article: This work was supported in part by the National Science Foundation under grant CMMI-1254262.

References

Agarwal BD, Broutman LJ and Chandrashekhara K (2006) *Analysis and Performance of Fiber Composites*. Hoboken, NJ: John Wiley & Sons.

Anton S, Erturk A and Inman D (2010) Multifunctional self-charging structures using piezoceramics and thin-film batteries. *Smart Materials and Structures* 19: 115021.

Baz A and Ro J (1996) Vibration control of plates with active constrained layer damping. *Smart Materials and Structures* 5: 272.

Beckert W and Kreher WS (2003) Modelling piezoelectric modules with interdigitated electrode structures. *Computational Materials Science* 26: 36–45.

Belloli A, Niederberger D, Pietrzko S, et al. (2007) Structural vibration control via RL shunted active fiber composites. *Journal of Intelligent Material Systems and Structures* 18: 275–287.

Bent AA (1997) *Active Fiber Composites for Structural Actuation*. Cambridge, MA: Massachusetts Institute of Technology.

Bent AA and Hagood NW (1997) Piezoelectric fiber composites with interdigitated electrodes. *Journal of Intelligent Material Systems and Structures* 8: 903–919.

Bent AA, Hagood NW and Rodgers JP (1995) Anisotropic actuation with piezoelectric fiber composites. *Journal of Intelligent Material Systems and Structures* 6: 338–349.

Berger H, Kari S, Gabbert U, et al. (2005) An analytical and numerical approach for calculating effective material coefficients of piezoelectric fiber composites. *International Journal of Solids and Structures* 42: 5692–5714.

Bilgen O, Kochersberger KB, Inman DJ, et al. (2010) Novel, bidirectional, variable-camber airfoil via macro-fiber composite actuators. *Journal of Aircraft* 47: 303–314.

Bowen C, Nelson L, Stevens R, et al. (2006) Optimisation of interdigitated electrodes for piezoelectric actuators and active fibre composites. *Journal of Electroceramics* 16: 263–269.

Brei D and Cannon BJ (2004) Piezoceramic hollow fiber active composites. *Composites Science and Technology* 64: 245–261.

Browning JS, Cobb RG, Canfield RA, et al. (2009) *F-16 ventral fin buffet alleviation using piezoelectric actuators*. Master's Thesis, Air Force Institute of Technology, Wright-Patterson Air Force Base, OH.

Cen L and Erturk A (2013) Bio-inspired aquatic robotics by untethered piezohydroelastic actuation. *Bioinspiration & Biomimetics* 8: 016006.

Cha Y, Chae W, Kim H, et al. (2016) Energy harvesting from a piezoelectric biomimetic fish tail. *Renewable Energy* 86: 449–458.

Cha Y, Kim H and Porfiri M (2013) Energy harvesting from underwater base excitation of a piezoelectric composite beam. *Smart Materials and Structures* 22: 115026.

Choi W, Jeon Y, Jeong J-H, et al. (2006) Energy harvesting MEMS device based on thin film piezoelectric cantilevers. *Journal of Electroceramics* 17: 543–548.

Collet M, Ruzzene M and Cunefare K (2011) Generation of Lamb waves through surface mounted macro-fiber composite transducers. *Smart Materials and Structures* 20: 025020.

Cunefare KA, Skow E, Erturk A, et al. (2013) Energy harvesting from hydraulic pressure fluctuations. *Smart Materials and Structures* 22: 025036.

Deraemaeker A and Nasser H (2010) Numerical evaluation of the equivalent properties of macro fiber composite (MFC) transducers using periodic homogenization. *International Journal of Solids and Structures* 47: 3272–3285.

Deraemaeker A, Nasser H, Benjeddou A, et al. (2009) Mixing rules for the piezoelectric properties of macro fiber composites. *Journal of Intelligent Material Systems and Structures* 20: 1475–1482.

Dosch JJ, Inman DJ and Garcia E (1992) A self-sensing piezoelectric actuator for collocated control. *Journal of Intelligent Material Systems and Structures* 3: 166–185.

Erturk A (2012) Assumed-modes modeling of piezoelectric energy harvesters: Euler–Bernoulli, Rayleigh, and Timoshenko models with axial deformations. *Computers & Structures* 106: 214–227.

Erturk A and Delporte G (2011) Underwater thrust and power generation using flexible piezoelectric composites: an experimental investigation toward self-powered swimmer-sensor platforms. *Smart Materials and Structures* 20: 125013.

Erturk A and Inman DJ (2009) An experimentally validated bimorph cantilever model for piezoelectric energy harvesting from base excitations. *Smart Materials and Structures* 18: 025009.

Erturk A and Inman DJ (2011a) Parameter identification and optimization in piezoelectric energy harvesting: analytical relations, asymptotic analyses, and experimental validations. *Proceedings of the Institution of Mechanical Engineers, Part I: Journal of Systems and Control Engineering* 225: 485–496.

Erturk A and Inman DJ (2011b) *Piezoelectric Energy Harvesting*. Chichester: Wiley.

Feenstra J, Granstrom J and Sodano H (2008) Energy harvesting through a backpack employing a mechanically amplified piezoelectric stack. *Mechanical Systems and Signal Processing* 22: 721–734.

Hagood NW and Von Flotow A (1991) Damping of structural vibrations with piezoelectric materials and passive electrical networks. *Journal of Sound and Vibration* 146: 243–268.

Hagood NW, Chung WH and von Flotow A (1990) Modeling of piezoelectric actuator dynamics for active structural control. *Journal of Intelligent Material Systems and Structures* 1: 327–354.

Hagood NW, Kindel R, Ghandi K, et al. (1993) Improving transverse actuation of piezoceramics using interdigitated surface electrodes. In: *1993 North American conference on smart structures and materials*, Albuquerque, NM, 1 February, pp. 341–352. Bellingham, WA: International Society for Optics and Photonics.

High JW and Wilkie WK (2003) Method of fabricating NASA-standard macro-fiber composite piezoelectric actuators. Available at: http://ismart-sms.org/upload/1458742414.pdf

Jeon Y, Sood R, Jeong J-H, et al. (2005) MEMS power generator with transverse mode thin film PZT. *Sensors and Actuators A: Physical* 122: 16–22.

Kim D-K and Han J-H (2006) Smart flapping wing using macrofiber composite actuators. In: *SPIE 6173, smart structures and materials 2006: smart structures and integrated systems*, San Diego, CA, 26 February–2 March, paper no. 61730F. Bellingham, WA: International Society for Optics and Photonics.

Kim D-K, Kim H-I, Han J-H, et al. (2007) Experimental investigation on the aerodynamic characteristics of a biomimetic flapping wing with macro-fiber composites. *Journal of Intelligent Material Systems and Structures*. Epub ahead of print 21 December. DOI: 10.1177/1045389X07083618.

Leadenham S and Erturk A (2015a) Nonlinear M-shaped broadband piezoelectric energy harvester for very low base accelerations: primary and secondary resonances. *Smart Materials and Structures* 24: 055021.

Leadenham S and Erturk A (2015b) Unified nonlinear electroelastic dynamics of a bimorph piezoelectric cantilever for energy harvesting, sensing, and actuation. *Nonlinear Dynamics* 79: 1727–1743.

Leo DJ (2007) *Engineering Analysis of Smart Material Systems*. Hoboken, NJ: John Wiley & Sons.

Lesieutre GA (1998) Vibration damping and control using shunted piezoelectric materials. *The Shock and Vibration Digest* 30: 187–195.

Lesieutre GA, Ottman GK and Hofmann HF (2004) Damping as a result of piezoelectric energy harvesting. *Journal of Sound and Vibration* 269: 991–1001.

Lin Y and Sodano HA (2008) Concept and model of a piezoelectric structural fiber for multifunctional composites. *Composites Science and Technology* 68: 1911–1918.

Lin Y and Sodano HA (2009) Electromechanical characterization of a active structural fiber lamina for multifunctional composites. *Composites Science and Technology* 69: 1825–1830.

Matt HM and Di Scalea FL (2007) Macro-fiber composite piezoelectric rosettes for acoustic source location in complex structures. *Smart Materials and Structures* 16: 1489.

Paradies R and Ciresa P (2009) Active wing design with integrated flight control using piezoelectric macro fiber composites. *Smart Materials and Structures* 18: 035010.

Prasath SS and Arockiarajan A (2015) Experimental and theoretical investigation on the thermo-electro-elastic properties of macro-fiber composites (MFC). *Composite Structures* 122: 8–22.

Shahab S and Erturk A (2014a) Contactless ultrasonic energy transfer for wireless systems: acoustic-piezoelectric structure interaction modeling and performance enhancement. *Smart Materials and Structures* 23: 125032.

Shahab S and Erturk A (2014b) Electrohydroelastic dynamics of macro-fiber composites for underwater energy harvesting from base excitation. In: *SPIE smart structures and materials + nondestructive evaluation and health monitoring*, San Diego, CA, 9–13 March, paper no. 90570C. Bellingham, WA: International Society for Optics and Photonics.

Shahab S and Erturk A (2014c) Underwater dynamic actuation of macro-fiber composite flaps with different aspect ratios: electrohydroelastic modeling, testing, and characterization. In: *ASME 2014 conference on smart materials, adaptive structures and intelligent systems*, Newport, RI, 8–10 September, p. V002T06A007 (9 pp.). New York: American Society of Mechanical Engineers.

Shahab S and Erturk A (2015a) Experimentally validated nonlinear electrohydroelastic Euler-Bernoulli-Morison

model for macro-fiber composites with different aspect ratios. In: *ASME 2015 international design engineering technical conferences and computers and information in engineering conference*, Boston, MA, 2–5 August, p. V008T13A030 (11 pp.). New York: American Society of Mechanical Engineers.

Shahab S and Erturk A (2015b) Unified electrohydroelastic investigation of underwater energy harvesting and dynamic actuation by incorporating Morison's equation. In: *SPIE smart structures and materials + nondestructive evaluation and health monitoring*, San Diego, CA, 8–12 March, paper no. 94310C. Bellingham, WA: International Society for Optics and Photonics.

Shahab S, Gray M and Erturk A (2015a) Ultrasonic power transfer from a spherical acoustic wave source to a free-free piezoelectric receiver: modeling and experiment. *Journal of Applied Physics* 117: 104903.

Shahab S, Tan D and Erturk A (2015b) Hydrodynamic thrust generation and power consumption investigations for piezoelectric fins with different aspect ratios. *The European Physical Journal: Special Topics* 224: 3419–3434.

Skow E, Cunefare K and Erturk A (2014) Power performance improvements for high pressure ripple energy harvesting. *Smart Materials and Structures* 23: 104011.

Smits JG and Choi W-S (1991) The constituent equations of piezoelectric heterogeneous bimorphs. *IEEE Transactions on Ultrasonics, Ferroelectrics, and Frequency Control* 38: 256–270.

Sodano HA, Park G and Inman DJ (2004) An investigation into the performance of macro-fiber composites for sensing and structural vibration applications. *Mechanical Systems and Signal Processing* 18: 683–697.

Stanton SC, Erturk A, Mann BP, et al. (2010) Resonant manifestation of intrinsic nonlinearity within electroelastic micropower generators. *Applied Physics Letters* 97: 254101.

Usher T and Sim A (2005) Nonlinear dynamics of piezoelectric high displacement actuators in cantilever mode. *Journal of Applied Physics* 98: 064102.

Wilkie WK, Bryant RG, High JW, et al. (2000) Low-cost piezocomposite actuator for structural control applications. In: *SPIE's 7th annual international symposium on smart structures and materials*, Newport Beach, CA, 6 March, pp. 323–334. Bellingham, WA: International Society for Optics and Photonics.

Williams RB, Grimsley BW, Inman DJ, et al. (2002) Manufacturing and mechanics-based characterization of macro fiber composite actuators. In: *ASME 2002 international mechanical engineering congress and exposition*, New Orleans, LA, 17–22 November, pp. 79–89. New York: American Society of Mechanical Engineers.

Williams RB, Inman DJ and Wilkie WK (2004a) Temperature-dependent thermoelastic properties for macro fiber composite actuators. *Journal of Thermal Stresses* 27: 903–915.

Williams RB, Inman DJ, Schultz MR, et al. (2004b) Nonlinear tensile and shear behavior of macro fiber composite actuators. *Journal of Composite Materials* 38: 855–869.

Wolf K and Gottlieb O (2002) Nonlinear dynamics of a noncontacting atomic force microscope cantilever actuated by a piezoelectric layer. *Journal of Applied Physics* 91: 4701–4709.

Zhao S and Erturk A (2014) Deterministic and band-limited stochastic energy harvesting from uniaxial excitation of a multilayer piezoelectric stack. *Sensors and Actuators A: Physical* 214: 58–65.